

Research Article

Study of the Failure Mode of a Jointed Rock Mass due to a Stress Wave

Xi Kun Qian ¹ and Cong Cong Li²

¹Investment Project Management Institute of Dongbei University of Finance and Economics, Dalian 116024, China

²Jinan Urban Construction Group, Jinan 250000, China

Correspondence should be addressed to Xi Kun Qian; 451867306@qq.com

Received 28 April 2021; Accepted 6 July 2021; Published 16 July 2021

Academic Editor: Chunyang Zhang

Copyright © 2021 Xi Kun Qian and Cong Cong Li. This is an open access article distributed under the Creative Commons Attribution License, which permits unrestricted use, distribution, and reproduction in any medium, provided the original work is properly cited.

The mechanical response and failure process of a jointed rock mass subjected to dynamic loading is very important for the safety and stability of rock engineering projects. In this study, we use RFPA2D-Dynamic, a rock dynamic failure process analysis platform, to establish a two-dimensional impact model of a jointed rock mass to analyze the mechanism of crack propagation in a jointed rock mass with preexisting cracks under dynamic loading. We discuss the influence of the stress wavelength and precrack inclination on the dynamic failure process and mode of the rock mass and compare this failure process with the failure model under static loading. The results show that the dynamic failure process and crack initiation type of a jointed rock mass are closely related to the stress wavelength. For a given peak, as the stress wavelength increases, the failure mode changes from local cracking that occurs above the precracks to a global instability caused by wing cracks. Meanwhile, as the wavelength increases, the shear cracks and mixed tensile-shear cracks generated at the two ends of the precracks are replaced by tensile cracks. The precrack inclination on a jointed rock mass mainly affects the strength of the jointed rock mass and the final failure mode. Specifically, when the joint inclination is small, the rock mass is severely damaged in the region above the precracks because the stress wave forms a region of cracks with a concentrated distribution. As the joint inclination increases, the damaged region becomes larger while the rock mass is less prone to failure; the strength of the rock mass gradually increases, and the wing cracks produced at the two ends of precracks propagate toward the upper and lower ends of the rock mass. However, when the stress wavelength is small, the precracks of different inclinations form cracks in the region above the precracks with a length similar to the precracks. For this condition, the propagation of the cracks is mainly controlled by the stress wavelength, while the influence of the inclination of the precracks is not significant. There is a significant difference between the failure modes of a rock specimen under dynamic loading or static loading because the stress wave produces a reflected tension wave in the direction parallel to the wave attack of the joint plane, which leads to spalling, while the wing cracks are more likely to occur under static loading.

1. Introduction

Because the jointed rock mass is a type of nonhomogeneous material, its failure process not only relies on the stress wavelength but is also related to the distribution of its internal joints [1, 2]. Therefore, studying the patterns of crack propagation of a jointed rock mass with different wavelengths and precrack inclinations has both theoretical significance and engineering value.

Rock masses are generally characterized by discontinuities such as fractures, joints, pores, and other original

defects that influence their mechanical properties and fracture behavior of rocks in the stability assessments of rock engineering. The failure of rock masses is usually associated with fractures propagation along preexisting flaw, because it often induces the initiation of cracking [3–8]. Moreover, it is well known that the loading rate also plays a crucial important role in the mechanical properties during the dynamic failure processes [9–12]. Therefore, a systematic study of the mechanisms of crack initiation and propagation processes in rock masses under dynamic loading condition promises benefit in many areas from

rock mechanics to mining engineering and earth quake prediction.

In recent decades, many laboratory experimental and numerical investigations have been well conducted to study crack initiation, propagation, and coalescence in rock and rock-like materials under static loading. For instance, papers [13–15] investigated the strength and cracking behaviors of rock and rock-like material containing single or multiple preexisting flaws under static loading condition. With regard to the dynamic investigations, they are extensively researched to study the dynamic mechanical properties of intact rock specimens under dynamic loading [16–23]. However, not so well understood is the dynamic failure process, which is closely related to crack behavior in terms of initiation, propagation and coalescence of cracks when the rock specimen is undertook different loading conditions. There have been few studies researching dynamic crack behaviors in rock specimen under different loading ratios [24–27]. For instance, Yang et al. [26] studied the mechanism of crack branching and curving in rock-like material under dynamic biaxial. They found that the loading ratio, crack dip angle, and material heterogeneity play a significant role in crack curving and branching. The loading ration, which is the load in horizontal and vertical direction, controls the crack curving. The crack dip angle and heterogeneity of the material are the decisive factor on the tensile properties and failure patterns of heterogeneity material with internal defects. Li and Wong [28] researched the crack initiation and propagation from preexisting flaw specimens under different loading conditions. The results indicate that different loading condition would produce different resultant crack types, crack initiation sequences, and crack pattern. Tensile cracks would tend to initiate prior to shear cracks under a relatively low loading rate. Meanwhile, the effect of flaw dip angle on the dynamic failure processes is also investigated by some researchers. Several researchers hold the view that the flaw dip angle has a limited influence on the crack propagation modes [29–33]. For instance, Li et al. [32] conducted dynamic loading tests using a modified split-Hopkinson pressure bar device to study the effects of preexisting flaws with different flaw angles and lengths on the dynamic failure processes. They have found that the geometry of the flaws appears to have a slight effect on failure patterns of flawed specimens. Zou et al. [30] revealed the effect of the flaw dip angle on crack trajectories during the dynamic failure processes by the SHPB. According to the experimental results, the effect of the flaw dip angle on the development of macrocracks is very limited under impact loadings. However, other researchers thought that there are significant influences of the flaw dip angle on the crack behaviors [27, 34–36]. Li et al. [37] numerically investigated the failure process of intermittent jointed rock mass subjected to dynamic loading. The failure characteristics of intermittent jointed rock mass with different flaw dip angles are simulated. The numerical results imply that the failure process is closely related to the dip angle of flaw. With the increase of the flaw dip angle, the damage range expands and the rock mass is more difficult to initiate new cracks. Besides, the fracture effect of rock mass with a flaw

dip angle of 45° – 60° is the best. In view of these arguments, further study of the effect of the flaw dip angle on the dynamic process in flawed specimen under a wide range of loading rates is essential to illuminate the relationship of these two factors. In addition, the similarities and differences of the crack propagation patterns on the specimen containing a preexisting flaw subjected to static and dynamic loading conditions have been summarized by several researchers [29, 31, 37, 38], whereas difference of the crack propagation patterns under static and dynamic loading conditions still needs more detailed research.

In this study, we select the dynamic analysis system of RFPA dynamic to conduct numerical experiments on the dynamic characteristics of a jointed rock mass and investigate the influence of the stress wavelength and joint inclination on the dynamic failure of a rock mass as well as the difference in the failure modes of a jointed rock mass with different preset inclinations under dynamic loading and static loading. We also discuss in depth the relationship between the influence of the stress wavelength on the type of initiation cracks and the influence of the wavelength and inclination on the mode of crack propagation, thus providing a reference for the design of relevant rock mass engineering projects.

2. Verification of the Numerical Method and Model Setup

2.1. Verification of the Numerical Method. The RFPA-dynamic analytical system used in this study can simulate the cracking process of a brittle nonhomogeneous material such as rock under dynamic loading. Details about the RFPA-dynamic software can be found in the literature [26, 39].

To ensure the accuracy and comparability of simulation results, we first verify the accuracy of numerical simulation results comparing them with results from a physical experiment in the literature [31]. The experiment utilized a horizontal impact test platform with a split Hopkinson pressure bar (SHPB) with a diameter of 50 mm to evaluate a brittle, rock-like material. The macroscopic modulus of elasticity, uniaxial compressive strength, and Poisson's ratio of the specimen were 4.5 GPa, 25.5 MPa, and 0.2, respectively. Figure 1 compares the results from the numerical simulation and physical experiment of the precracked specimen with the SHPB. We can see that the numerical simulation satisfactorily reproduces the crack propagation mode of the rock specimen under an impact load and reveals an "X"-type final failure mode, which is consistent with the experimental result.

To validate the feasibility of the numerical method on simulating the stress wave propagation characteristics, the SHPB test on limestone by Frew et al. [40] is selected. The geometric and material parameters of the SHPB model are consistent with those in the literature. The length of impact bar, incident bar, transmission bar, and rock sample is 152 mm, 2130 mm, 915 mm, and 12.5 mm, respectively, and the diameter is 12.5 mm. The schematic diagram of the model is shown in Figure 2. To maximize computational efficiency based on guaranteed accuracy, the element size is

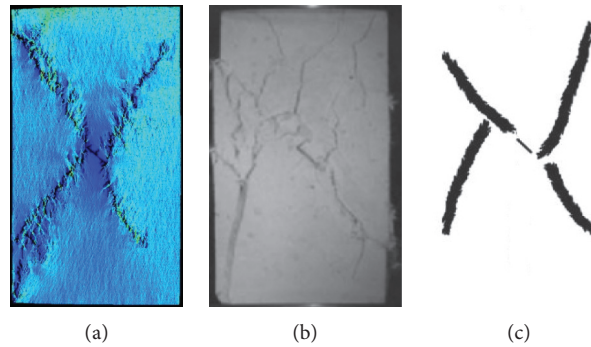


FIGURE 1: Comparison of numerical and experimental rock failure modes for SHPB.

selected as 0.5 mm according to the findings by Liao et al. [41]. Meanwhile, the impact bar, incident bar, and transmission bar are homogeneous materials, and the rock homogeneity coefficient is 4. In addition, the right boundary of the transmission bar is set with artificial absorption boundary to eliminate the influence of the reflected stress wave on the monitoring results. The monitoring points are located on the incident bar and the transmission bar, respectively, which is consistent with the literature. The mechanical parameters of rock and bar are shown in Table 1.

Through comparison between the reflected wave histories measured by Frew and the simulation results, as shown in Figure 3, good agreement can be found. It is found that the waveforms of incident wave, reflected wave, and transmitted wave obtained by numerical simulation and experiment are in good agreement. However, the stress waves in the simulated test are slightly greater than that in the laboratory experiment. This is because the impact process is ideal in the simulation, which ignores the roughness at the impact interface between the rock specimen and bars. The results indicate that the RFPA can simulate the stress wave propagation in dynamic loading process. Therefore, in the present study, this numerical code, which is able to simulate the responses of rock subjected to dynamic loading, is used.

2.2. Model Setup. The computational model employed in this study is shown in Figure 4. The size of the model is 50×100 mm, and the number of elements is $200 \times 400 = 80,000$. The computational model does not consider the influence of damping for the time being. A plane stress condition is assumed in the model, and all boundaries of the numerical rock samples are set as the free boundary, except the bottom one, which is set as viscoelastic absorption boundary. The specimen is fixed at the lower surface and subjected to a triangular compressive stress wave σ at the upper surface.

According to the modulus of elasticity and density of rock materials, we can calculate the propagation velocity of a one-dimensional longitudinal wave as 3,798 m/s. To study the influence of different stress wavelengths and peaks on the failure mode of the specimen, we apply the stress waves shown in Figure 5 to the numerical model. In Figure 5, the peaks of the stress waves I to IV are all 20 MPa, and the

wavelengths λ of the applied compressive stress waves I to IV are 7.6, 37.98, 75.96, and 189.9 mm, respectively. The time step size Δt is set to be $0.1 \mu\text{s}$ in the calculation. To fully consider the propagation and action time of the stress wave inside the rock mass, the time t needed for a specimen to end its dynamic response is $70 \mu\text{s}$ in the calculation.

To study the influence of the precrack inclination on the failure mode of the specimen, we set the precrack to be an unfilled pore element, which is located in the middle of a specimen. To reduce the influence of the precrack size, we set the precrack to be 15 mm long and 0.5 mm wide. The crack inclination α is 0° , 15° , 30° , 45° , 60° , 75° , or 90° .

The matrix elements in the model of this study have an average compressive strength of 205 MPa, average modulus of elasticity of 37.5 GPa, degree of homogeneity of 3, density of $2,600 \text{ kg/m}^3$, friction angle of 50° , Poisson's ratio of 0.25, compression-tension strength ratio of 10, damping factor of 0 (i.e., the influence of damping is not considered), and time step of $0.1 \mu\text{s}$. The model has a free boundary, and a plane stress analysis is adopted.

3. Analysis of the Calculated Results

3.1. Influence of the Stress Wavelength on the Failure Process of a Rock Mass. Herein we use the example of $\alpha = 45^\circ$ and the peak of the stress wave is 20 MPa to discuss in detail the influence of the stress wavelength on the pattern of precrack propagation.

Figure 6(a) shows the distribution of the maximum shear stresses during the failure process of the rock mass specimen with precracks under stress wave I ($\lambda = 7.6$ mm). We can see from the simulation plot the whole process of the stress wave propagating at a certain velocity from the upper end to the lower end of the specimen. The color brightness of the elements in the figure reflects the relative magnitude of the elemental shear stress; a brighter position means a larger maximum shear stress at that location. The influence of the reflection on the two side boundaries of the rock specimen is considered. As the stress wave propagates downward, the stress waves are reflected and superposed on the side boundaries and act jointly with the applied compressive stress wave on the rock specimen. The propagation of the stress wave is accompanied by the failure of elements, which also changes the distribution of the stress field. When the

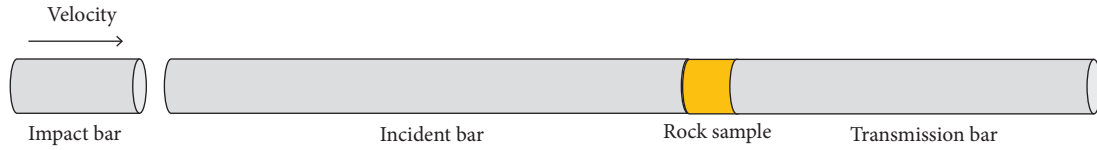


FIGURE 2: Schematic diagram of SHPB numerical model.

TABLE 1: The material properties of SHPB tests.

	E (GPa)	ν	σ (MPa)	ρ (kg/m ³)
Rock sample	24	0.23	67	2650
SHPB bar	200	0.28	2500	8100

stress wave propagates to the crack tip, a stress concentration occurs in the local zone, which causes a damaged and failing element to appear. As the stress wave continues to propagate, the number of damaged elements at the crack tip gradually increases, and the damaged elements coalesce to form wing cracks that are perpendicular to the precrack. In addition, the presence of joints changes the propagation path of the stress wave, and the stress wave is reflected at the crack, which causes the compressive stress wave to become a tensile stress wave and leads to a spalling failure above the precrack plane. Meanwhile, the cracks undergo close contact under a compressive stress wave when the stress wave transmission occurs at the crack. As the stress wave continues to propagate downward, the tension-damaged elements gradually appear in the region parallel to and above the precrack. They develop into fine cracks and finally coalesce to form a macroscopic crack, which is parallel to and has a similar length of the precrack, indicating that the failure mode of a rock mass is closely related to the existing joint cracks inside the rock mass.

From the diagram of the maximum shear stress distribution shown in Figure 6(b), we can clearly see the failure process and stress distribution of the rock specimen when its upper surface is subjected to stress wave II ($\lambda = 37.98$ mm). Due to the difference of the stress wavelength, the initiation and propagation of cracks in the rock specimen are different from those of the specimen under stress wave I ($\lambda = 7.6$ mm):

- (1) The stress waves reflected on the two sides of the specimen are superposed in the middle of the upper end of the specimen, causing a failure in the middle of the specimen top end. As the stress wave propagates downward, the superposition position of the stress waves continuously moves downward, and the damaged elements gradually coalesce to form a macroscopic crack, which appears almost simultaneously as the wing crack perpendicular to the tip of the precrack, as shown in Figure 6(b). As the energy of the stress wave continuously attenuates during the propagation process, the intensity of the tensile stress wave that is reflected and superposed on the two sides gradually decreases, and the crack at the upper end of specimen develops to a certain extent and then stops.

- (2) The wing crack perpendicular to the precrack tip appears; the densely distributed short and small cracks appear in the region parallel to and above the precrack, and they gradually coalesce to form a local fractured region.
- (3) A macroscopic wing crack perpendicular to the lower end of the precrack is formed at the lower end of the crack. When a wing crack develops to a certain length, its direction gradually aligns itself with the direction of the external loading. When the stress wave propagates to the lower end of the specimen, it is reflected and refracted, which leads to failure of the new elements at the lower end of the specimen gradually developing into fine cracks. As the reflected stress wave propagates upward, the cracks at the lower end of specimen develop upward, and, therefore, a concentrated failure zone appears at the lower end of the specimen.

When stress wave III ($\lambda = 75.96$ mm) is applied to the upper surface of the rock specimen, the distribution of the maximum shear stress, as shown in Figure 6(c), shows that the crack propagation of the rock mass is similar but different than that under stress wave II ($\lambda = 37.98$ mm). The crack in the upper end of the specimen produced by the tensile stress wave reflected by the two sides of the specimen is longer, as shown in Figure 6(c). The wing crack perpendicular to the tip of the precrack continuously develops and propagates with the stress wave in the rock specimen and gradually connects with the crack in the upper end of the specimen. Meanwhile, the wing crack generated at the lower end of the precrack continuously develops downward, with its direction gradually aligning with the direction of the external loading, and it gradually connects to the fractured region produced by the tensile stress wave reflected at the lower end of the specimen. The wing crack eventually coalesces to form two macroscopic cracks through the upper and lower ends of the specimen.

When the stress wavelength continues to increase to a certain level ($\lambda = 189.9$ mm), as shown in Figure 6(d), the final failure mode of the specimen is similar to that under static loading. A wing crack perpendicular to the precrack is gradually produced at the upper and lower ends of the precrack, and it gradually propagates to the upper and lower

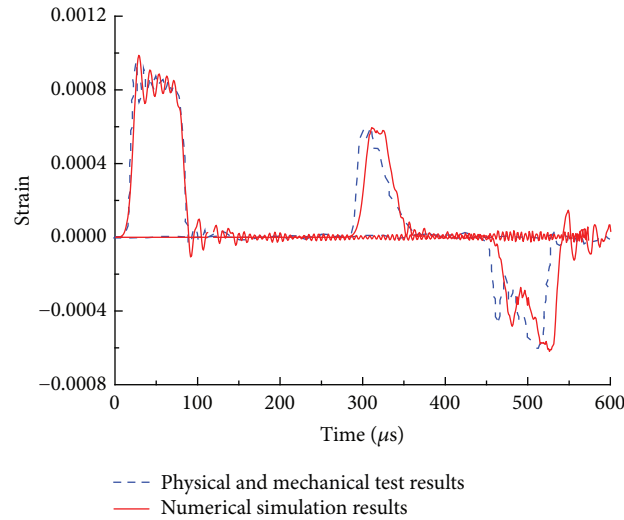


FIGURE 3: Comparison of numerical and experimental stress wave waveforms for SHPB impact test.

ends of the specimen. The development direction of the wing crack gradually aligns itself with the direction of the external loading and eventually forms two macroscopic cracks.

The maximum shear stress diagram in Figure 6 clearly shows the influence of the stress wavelength on the crack propagation and failure mode of the rock mass. As shown in Figure 6(a), when the stress wavelength is short ($\lambda = 7.6$ mm), a new crack is initiated parallel to and above the precrack, and its length is similar to that of the precrack. As the stress wavelength continues to increase, the wing cracks perpendicular to the precrack appear at the upper and lower ends of the precrack, and they expand and coalesce toward the upper and lower ends of the rock specimen. When the stress wavelength increases to a certain length, the final failure mode of the specimen is similar to that under static loading.

3.2. Failure Process of the Rock Mass with Different Precrack Inclinations. To study the influence of different inclinations of the precrack on the crack propagation and failure process of rock mass, we apply stress wave II to the upper surface of the fractured rock mass with precrack inclinations α of 0° , 15° , 30° , 45° , 60° , 75° , and 90° .

We use three failure mode types corresponding to 0° , 30° , and 75° for a detailed discussion. Different inclinations of the precrack change the propagation direction of the stress wave, thus leading to different crack propagation modes. The diagram of the maximum shear stress for the failure process of the rock specimen with a precrack inclination $\alpha = 0^\circ$ is shown in Figure 7. As the stress wave propagates inside the rock mass, the tensile stress wave and the subsequent stress wave reflected by the precrack plane are superposed in the upper part of the precrack plane, forming a tensile failure zone, and the damaged elements gradually increase to form macroscopic cracks. The newly generated macroscopic cracks are approximately parallel to the precrack plane and distributed in layers from near to far relative to the precrack plane and their lengths are similar to that of the precrack. In

particular, the two ends of the new cracks closest to the precrack plane gradually connect to the two ends of the precrack and form a closed failure zone. Meanwhile, the failure of the rock mass below the precrack plane is initiated by gradual generation of a macroscopic crack nearly perpendicular to the surface of the precrack and from the middle of the precrack, which extends downward as the stress wave propagates in the rock mass. When α is 30° , the new cracks above the precrack are parallel to the precrack and approximately distributed in layers. The initiation direction of the new cracks under the precrack plane is perpendicular to the precrack, and the initiation position of the cracks gradually moves from the middle to the bottom of the precrack. As the inclination of the precrack continues to increase, the wing cracks perpendicular to the precrack are generated at the two tips of the precrack, and they gradually propagate toward the upper and lower ends of the rock specimen with the propagation of the stress wave. When the inclination of the precrack is 75° , the development of new cracks at the upper tip of the precrack is not significant, while the direction of new cracks at the lower tip of the precrack is nearly aligned with the direction of the external loading, as shown in Figure 7(c).

In this study, we also conduct a numerical simulation on the rock specimen with the precrack inclination of 15° , 45° , 60° , and 90° . The propagation mode of cracks with $\alpha = 15^\circ$ is similar to that with $\alpha = 0^\circ$ (Figure 7(a)). When the inclination of the precrack is 45° or 60° , the propagation of the wing crack at the lower end of the precrack initially exhibits a step-like zigzag, and then it tends to develop downward in the loading direction. Wing cracks perpendicular to the precrack are generated at the precrack tip and, as the precrack inclination gradually increases, the propagation direction of the wing cracks gradually inclines toward the top of the rock mass. When the precrack inclination α is 90° , the incident direction of the stress wave is parallel to the precrack, and the new cracks in the lower end of the precrack propagate along the existing precrack, while there is no obvious crack generated above the precrack. Figure 8 shows a diagram of

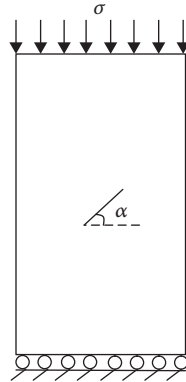


FIGURE 4: Geometrical parameters and loading conditions of rock specimen.

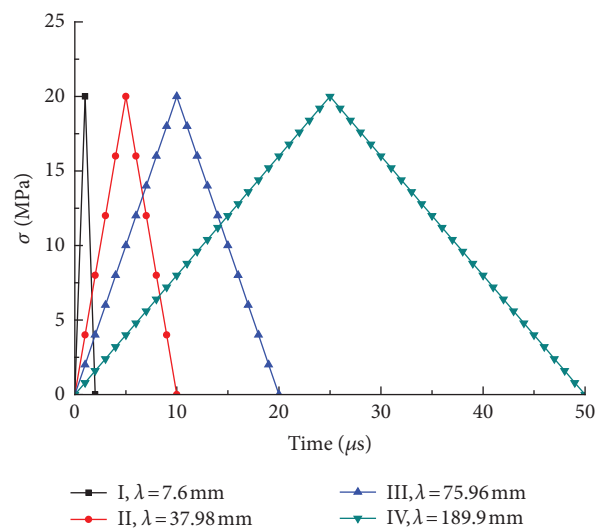


FIGURE 5: Stress waves applied on the rock specimen.

the final failure shear stress at $t = 30 \mu\text{s}$ for different inclinations. When $\alpha = 0^\circ$, cracks in the rock mass develop most significantly, which leads to the most severe failure. As the precrack inclination gradually increases, the degree of the rock mass failure also decreases, which indicates that the precrack inclination has an important influence on the response of the rock mass to dynamic loading.

3.3. Comparative Analysis of Failure Modes under Dynamic Loading and Static Loading. To compare the initiation, propagation, and coalescence process of cracks under both dynamic loading and static loading and to reveal the corresponding differences in failure modes of the specimens with precracks, we obtain through simulation the failure modes of rock specimens with different precrack inclinations under static loading, as shown in Figure 9. A displacement-controlled static loading rate of 0.003 mm/step is adopted.

We can see from Figure 9 that, under static loading, the cracks are initially closed under pressure, and the stress concentration occurs simultaneously at the two ends of the

crack. When the precrack inclination $\alpha = 0^\circ$, as the load increases, the failure occurs in the middle of the precrack and gradually develops upward and downward, eventually forming two macroscopic cracks aligned with the direction of the loading. As the precrack inclination gradually increases, new cracks are always initiated at the precrack tip and eventually form two macroscopic cracks through the upper and lower ends of the specimen. Through a comprehensive comparison, we obtain the following patterns:

- (1) The propagation mode of cracks under a relatively long stress wavelength is close to that under static loading.
- (2) The stress wave generates a reflected tension wave in the direction parallel to the wave attack of the joint plane, which leads to spalling, while wing cracks are more likely to occur under static loading.
- (3) The morphology of crack propagation under static loading has a symmetric distribution. Unlike static loading, the stress wave generates an asymmetric failure at the upper and lower ends of the specimen as well as above and below the cracks. Due to the

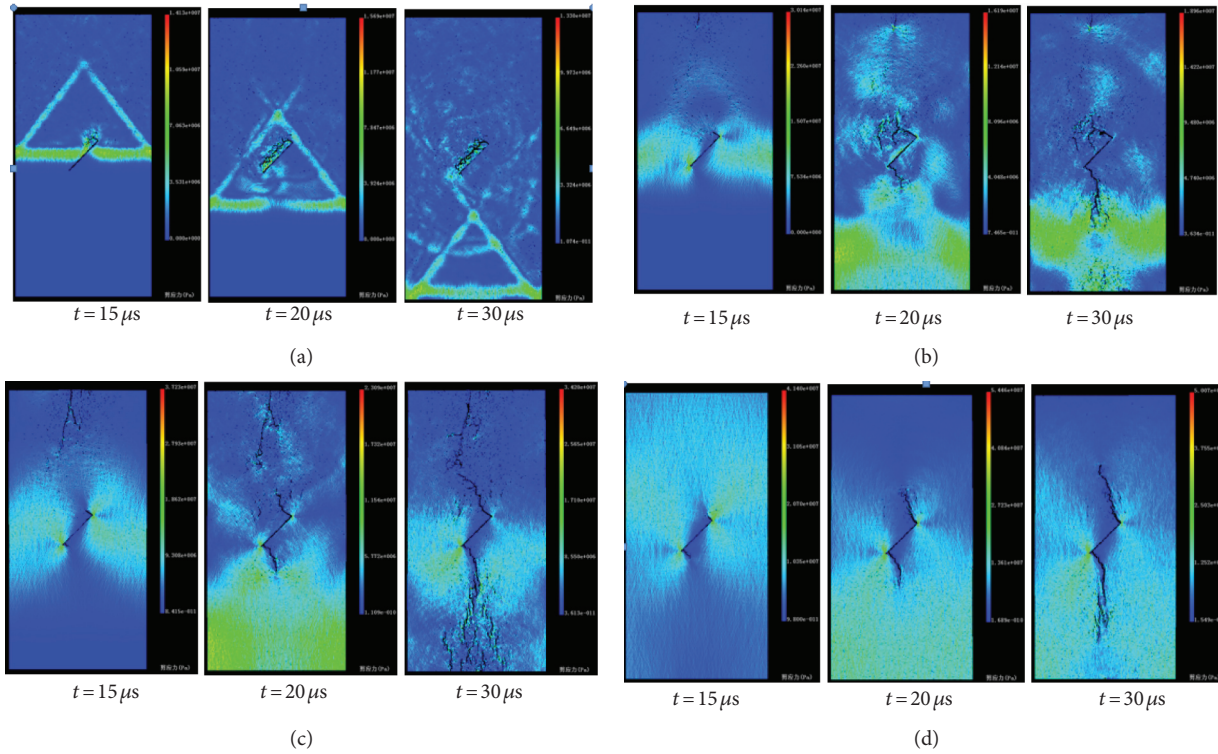


FIGURE 6: Failure process of flawed rock specimen with $\alpha = 45^\circ$ when subjected to stress wave from I to IV. (a) Failure process of flawed rock specimen with $\alpha = 45^\circ$ when subjected to stress wave I. (b) Failure process of flawed rock specimen with $\alpha = 45^\circ$ when subjected to stress wave II. (c) Failure process of flawed rock specimen with $\alpha = 45^\circ$ when subjected to stress wave III. (d) Failure process of flawed rock specimen with $\alpha = 45^\circ$ when subjected to stress wave IV.

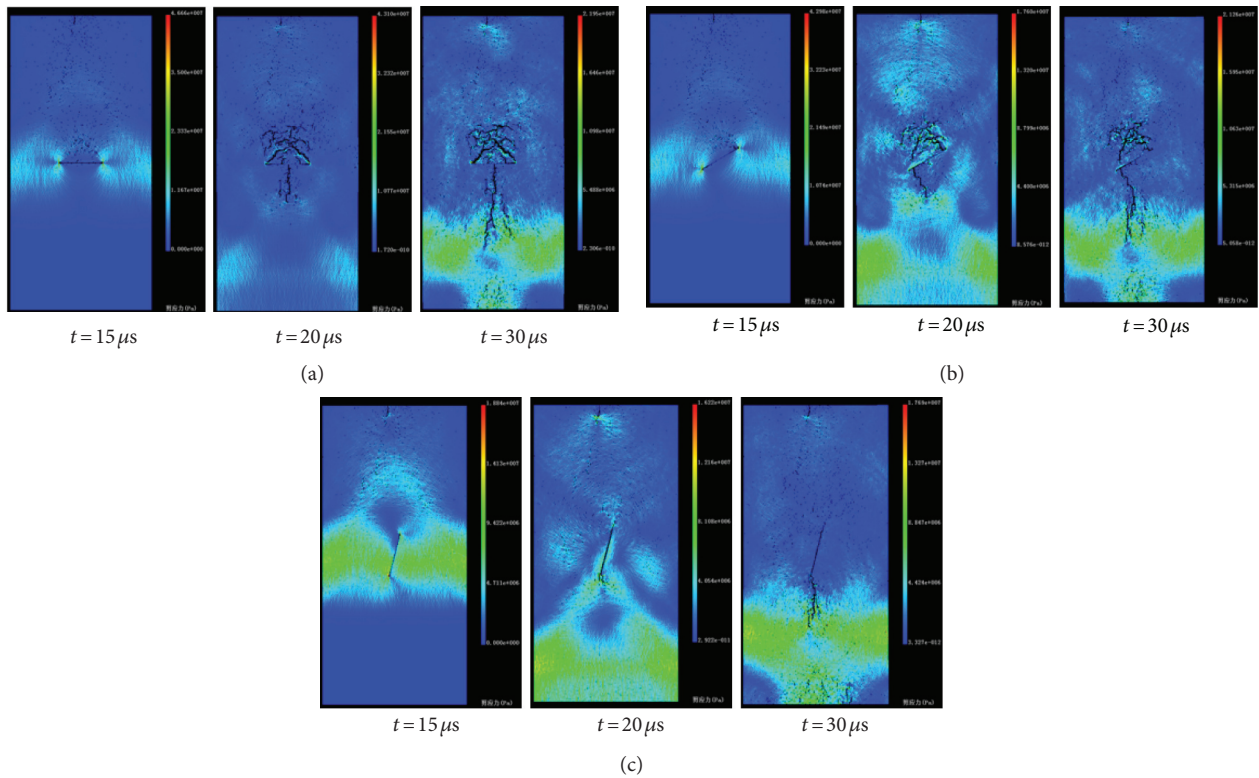


FIGURE 7: Failure process of rock specimen with different angle preexisting crack. (a) Failure process of flawed rock specimen with $\alpha = 0^\circ$ when subjected to stress wave II. (b) Failure process of flawed rock specimen with $\alpha = 30^\circ$ when subjected to stress wave II. (c) Failure process of flawed rock specimen with $\alpha = 75^\circ$ when subjected to stress wave II.

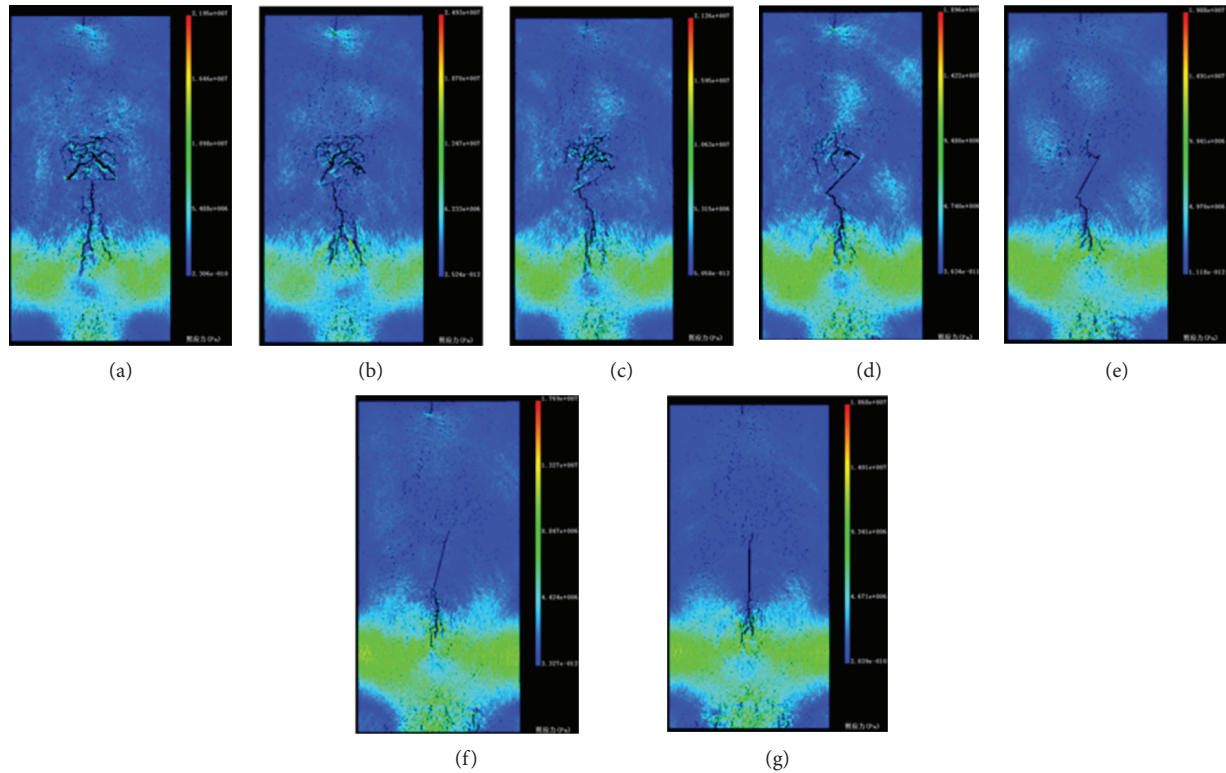


FIGURE 8: Failure patterns of rock specimens with different inclination angles of preexisting cracks when subjected to stress wave II. (a) $\alpha = 0^\circ$. (b) $\alpha = 15^\circ$. (c) $\alpha = 30^\circ$. (d) $\alpha = 45^\circ$. (e) $\alpha = 60^\circ$. (f) $\alpha = 75^\circ$. (g) $\alpha = 90^\circ$.

shielding effect of cracks, the stress wave is attenuated after passing through the cracks, which leads to changes in the propagation mode above and below the precrack.

- (4) Relative to static loading, the cracked rock mass under dynamic loading exhibits a stress field with a complicated distribution. Due to the shielding effect of cracks and the reflection effect of the boundaries, the stress waves inside the specimen under a dynamic loading undergo complicated interactions and thus exhibit a complicated distribution of the stress field.
- (5) The influence of the crack inclination on the dynamic and static strengths of a rock mass is also different. When the crack inclination varies in the range of 0° – 90° , the static strength of the specimen exhibits a U-shaped decrease-increase distribution curve. Under dynamic loading, as the inclination increases, the contact area between the stress wave and the crack inclination decreases and more energy is applied to the specimen, and, therefore, the rock mass strength monotonically increases.

4. Discussion

4.1. Influence of the Stress Wavelength on the Type of Cracks. The cracks produced around the precrack in the rock specimen under dynamic loading have different types of generated cracks for different wavelengths. Figure 10 shows the propagation modes of cracks in the rock

specimen under four different stress wavelengths. In reference to the crack type definition in Figure 11, we discuss the influence of different wavelengths on the type of generated cracks. When the rock mass is subjected to stress wave I, a large number of damaged elements appear parallel to and above the precrack plane in the region above the precrack, and the elements gradually coalesce to cause a spalling failure with a length similar to that of the precrack. When stress wave II acts on the cracked specimen, significant shear cracks are generated in the upper end of the precrack. As the wavelength increases, the crack type in the upper end of the precrack gradually evolves from a shear crack to a mixed tension-shear crack, and when stress wave IV is applied, the crack type completely evolves to a tensile crack. In the lower end of the precrack, different types of cracks also appear as the wavelength varies. Due to the reflection and attenuation of the stress wave, when only subjected to the stress wave II, a tensile crack occurs in the upper end of the precrack. Numerical simulation results reveal that, in combination with a long wavelength, the tensile crack is the main type of crack that appears around the precrack; as the wavelength decreases, the type of cracks gradually changes from tensile cracks to mixed tensile-shear cracks and then to shear cracks, which eventually leads to fracturing of the local region. Meanwhile, even if subjected to the same stress wave, due to the difference in positions, different types of cracks appear at the two ends of the precrack. Therefore, the stress wavelength and the relative position of the precrack

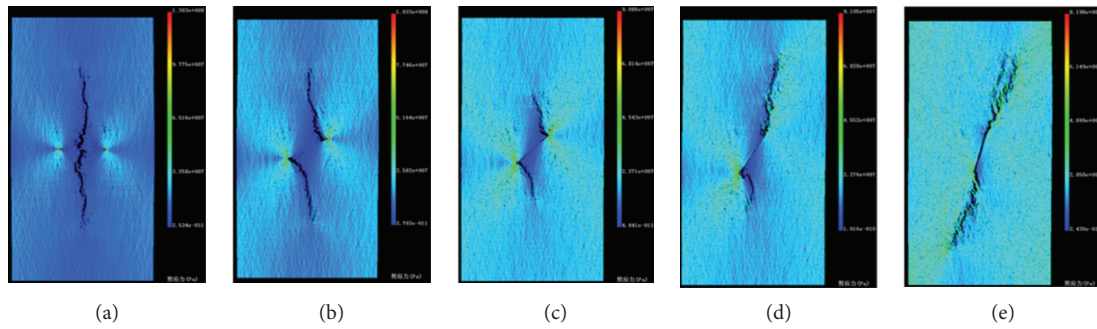


FIGURE 9: Failure patterns of rock specimens with different inclination angles of preexisting cracks under static loading. (a) $\alpha = 0^\circ$. (b) $\alpha = 30^\circ$. (c) $\alpha = 45^\circ$. (d) $\alpha = 60^\circ$. (e) $\alpha = 75^\circ$.

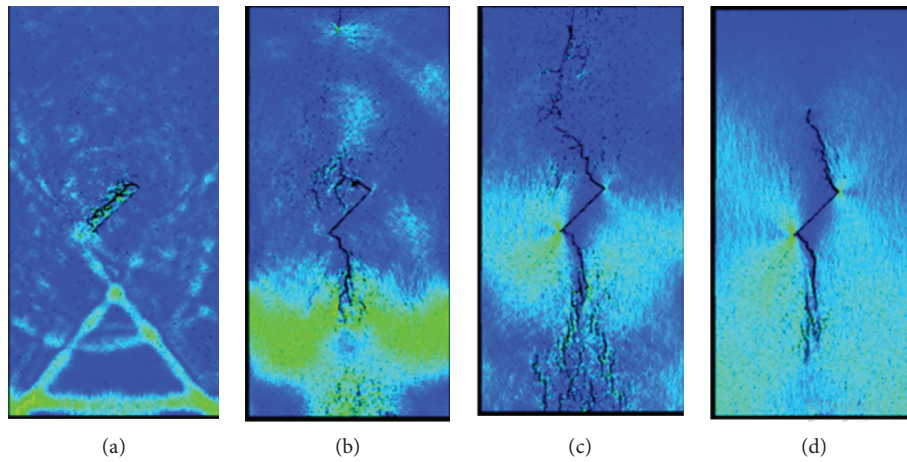


FIGURE 10: Failure patterns of rock specimen crack when subjected to stress wave from I to IV. (a) $\lambda = 7.6$ mm. (b) $\lambda = 37.98$ mm. (c) $\lambda = 75.96$ mm. (d) $\lambda = 189.9$ mm.

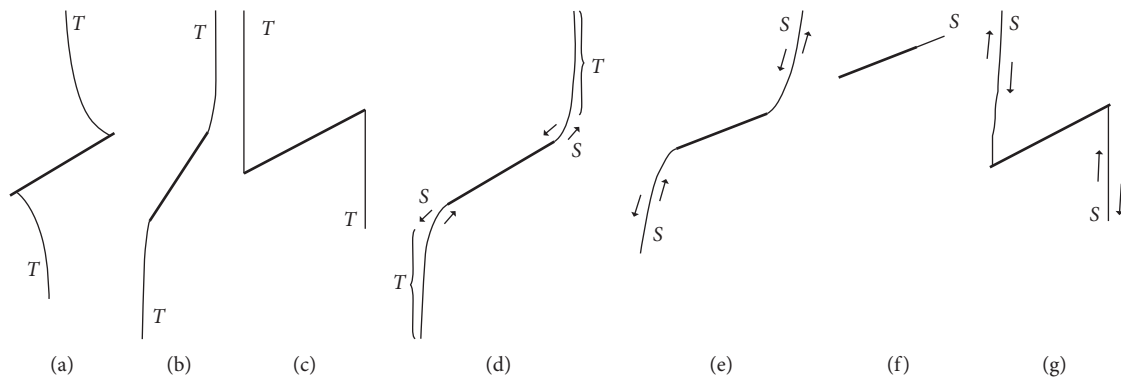


FIGURE 11: Various crack types initiated from the preexisting flaws identified [42]. *T*—tensile cracks. *S*—shear cracks. (a) Type 1 tensile crack (tensile wing crack). (b) Type 2 tensile crack. (c) Type 3 tensile crack. (d) Mixed tensile-shear crack. (e) Type 1 shear crack. (f) Type 2 shear crack. (g) Type 3 shear crack.

jointly determine the type of cracks that dominate specimen failure.

4.2. Influence of the Stress Wavelength and Pre-crack Inclination on the Propagation of Cracks in a Rock Mass. On the basis of previous studies, to illustrate the influence of the

stress wavelength and pre-crack inclination on the crack propagation mode of a rock mass, we simulate the failure process of rock specimens with pre-cracks for different inclinations under stress wave I as a supplemental study. Figure 12 shows a diagram of the shear stress at time $t = 20 \mu\text{s}$ for the rock specimen with pre-crack inclinations of 0° , 30° , and 60° under stress wave I. Although different from those

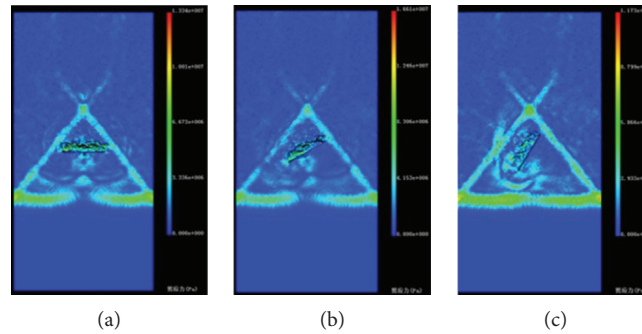


FIGURE 12: Failure process of rock specimen with different preexisting crack inclination angle when subjected to stress wave I. (a) $\alpha = 0^\circ$. (b) $\alpha = 30^\circ$. (c) $\alpha = 60^\circ$.

under stress wave II, the propagation modes of cracks in a rock mass under stress wave I are almost identical for the different precrack inclinations. As the stress wave propagates in the rock mass, the damaged elements appear parallel to and above the precrack plane and gradually coalesce to form a spalling failure with a length similar to that of the precrack. The failure mode of rocks is not significantly affected by the precrack inclination, and the level of failure gradually decreases as the precrack inclination increases. That is, when the stress wave applied above the rock specimen has a relatively short wavelength, the propagation of cracks is mainly controlled by the stress wavelength and is not significantly influenced by the precrack inclination.

5. Conclusions

- (1) The stress wavelength has a relatively large influence on the crack propagation and failure mode of a rock specimen. When the stress wavelength is short, the length of new cracks initiated parallel to and above the precrack is similar to that of the precrack. As the stress wavelength gradually increases, the wing cracks produced at the two ends of the precrack change from shear cracks to mixed tensile-shear cracks to tensile cracks. The failure mode changes from local failure to global instability. When the stress wavelength increases to a certain level, the failure mode of the rock specimen is rather close to that under static loading.
- (2) The morphology of the spatial distribution of joints has an important influence on the failure mode of a rock mass. The smaller the precrack inclination is, the larger the failure zone that occurs in the upper part of the cracks because the stress wave is reflected by the precrack and wing cracks appear at the lower end of the cracks. As the precrack inclination increases, the wing cracks perpendicular to the precrack are formed at the upper and lower tips of the precrack, and the propagation of cracks at the lower tip is more significant. As the inclination increases and the propagation of the stress wave is parallel to the crack surface, the rock mass is less vulnerable to failure. Otherwise, when the direction of the stress

wave is perpendicular to the crack plane, the rock mass is more vulnerable to failure.

- (3) Under dynamic loading and static loading, there is a significant difference in the failure modes of a rock specimen. The stress wave produces a reflected tension wave in the direction parallel to the wave attack of the joint plane, which leads to spalling, while the wing cracks are more likely to occur under static loading. The morphology of crack propagation under static loading is symmetrically distributed, while the stress wave leads to asymmetric failure at the upper and lower ends of the specimen as well as above and below the cracks.
- (4) Under a certain peak condition, when the shear wavelength is relatively short, the propagation of cracks is mainly controlled by the wavelength, and the precrack inclination has a relatively small influence on the propagation of cracks.

Data Availability

The data used to support the findings of this study are available from the corresponding author upon request.

Conflicts of Interest

The authors declare that they have no conflicts of interest regarding this paper.

Acknowledgments

This work was supported by the National Natural Science Foundation of China (grant nos. 51779031 and 51678170).

References

- [1] C. Y. Zhang, Y. X. Wang, and T. T. Jiang, "The propagation mechanism of an oblique straight crack in a rock sample and the effect of osmotic pressure under in-plane biaxial compression," *Arabian Journal of Geosciences*, vol. 13, no. 15, pp. 1–16, 2020.
- [2] X. S. Li, Z. F. Liu, and S. Yang, "Similar physical modeling of roof stress and subsidence in room and pillar mining of a gently inclined medium-thick phosphate rock," *Advances in Civil Engineering*, vol. 2021, pp. 1–17, 2021.

- [3] R. H. C. Wong, C. A. Tang, K. T. Chau, and P. Lin, "Splitting failure in brittle rocks containing pre-existing flaws under uniaxial compression," *Engineering Fracture Mechanics*, vol. 69, no. 17, pp. 1853–1871, 2002.
- [4] L. N. Y. Wong and H. Q. Li, "Numerical study on coalescence of two pre-existing coplanar flaws in rock," *International Journal of Solids & Structures*, vol. 50, no. 22-23, pp. 3685–3706, 2013.
- [5] X. P. Zhou, J. Bi, and Q. H. Qian, "Numerical simulation of crack growth and coalescence in rock-like materials containing multiple pre-existing flaws," *Rock Mechanics and Rock Engineering*, vol. 48, no. 3, pp. 1097–1114, 2015.
- [6] C. Y. Zhang, C. Z. Pu, R. H. Cao, T. Jiang, and G. Huang, "The stability and roof-support optimization of roadways passing through unfavorable geological bodies using advanced detection and monitoring methods, among others, in the Sanmenxia Bauxite Mine in China's Henan Province," *Bulletin of Engineering Geology and the Environment*, vol. 78, no. 7, pp. 5087–5099, 2019.
- [7] X. K. Qian, Z. Z. Liang, Z. Y. Liao, and K. Wang, "Numerical investigation of dynamic fracture in rock specimens containing a pre-existing surface flaw with different dip angles," *Engineering Fracture Mechanics*, vol. 223, Article ID 106675, 2019.
- [8] X. S. Li, S. Yang, Y. M. Wang, W. Nie, and Z. F. Liu, "Macro-micro response characteristics of surrounding rock and overlying strata towards the transition from open-pit to underground mining," *Geofluids*, vol. 2021, pp. 1–18, 2021.
- [9] S. H. Cho, Y. Ogata, and K. Kaneko, "Strain-rate dependency of the dynamic tensile strength of rock," *International Journal of Rock Mechanics and Mining Sciences*, vol. 40, no. 5, pp. 763–777, 2003.
- [10] F. Dai, R. Chen, and K. Xia, "A semi-circular bend technique for determining dynamic fracture toughness," *Experimental Mechanics*, vol. 50, no. 6, pp. 783–791, 2010.
- [11] F. Dai, K. Xia, H. Zheng, and Y. X. Wang, "Determination of dynamic rock Mode-I fracture parameters using cracked chevron notched semi-circular bend specimen," *Engineering Fracture Mechanics*, vol. 78, no. 15, pp. 2633–2644, 2011.
- [12] C. Y. Zhang, Y. X. Wang, H. Ruan, B. Ke, and H. Lin, "The strain characteristics and corresponding model of rock materials under uniaxial cyclic load/unload compression and their deformation and fatigue damage analysis," *Archive of Applied Mechanics*, vol. 91, no. 6, pp. 2481–2496, 2021.
- [13] R. H. C. Wong, M. L. Huang, M. R. Jiao, C. A. Tang, and W. S. Zhu, "The mechanisms of crack propagation from surface 3-D fracture under uniaxial compression," *Key Engineering Materials*, vol. 261–263, pp. 219–224, 2004.
- [14] H. Lee and S. Jeon, "An experimental and numerical study of fracture coalescence in pre-cracked specimens under uniaxial compression," *International Journal of Solids and Structures*, vol. 48, no. 6, pp. 979–999, 2011.
- [15] S. Y. Wang, S. W. Sloan, D. C. Sheng, and C. A. Tang, "Numerical analysis of the failure process around a circular opening in rock," *Computers and Geotechnics*, vol. 39, pp. 8–16, 2012.
- [16] X. B. Li, T. S. Lok, and J. Zhao, "Dynamic characteristics of granite subjected to intermediate loading rate," *Rock Mechanics and Rock Engineering*, vol. 38, no. 1, pp. 21–39, 2005.
- [17] S. Y. Wang, S. W. Sloan, H. Y. Liu, and C. A. Tang, "Numerical simulation of the rock fragmentation process induced by two drill bits subjected to static and dynamic (impact) loading," *Rock Mechanics and Rock Engineering*, vol. 44, no. 3, pp. 317–332, 2010.
- [18] F. Dai, S. Huang, K. Xia, and Z. Tan, "Some fundamental issues in dynamic compression and tension tests of rocks using split Hopkinson pressure bar," *Rock Mechanics and Rock Engineering*, vol. 43, no. 6, pp. 657–666, 2010.
- [19] S. Huang, K. Xia, and F. Dai, "Establishment of a dynamic mohr–coulomb failure criterion for rocks," *International Journal of Nonlinear Sciences and Numerical Simulation*, vol. 13, no. 1, pp. 55–60, 2012.
- [20] T. Kazerani, G. F. Zhao, and J. Zhao, "Dynamic fracturing simulation of brittle material using the distinct lattice spring method with a full rate-dependent cohesive law," *Rock Mechanics and Rock Engineering*, vol. 43, no. 6, pp. 717–726, 2010.
- [21] W. C. Zhu, Y. Bai, X. B. Li, and L. L. Niu, "Numerical simulation on rock failure under combined static and dynamic loading during SHPB tests," *International Journal of Impact Engineering*, vol. 49, pp. 142–157, 2012.
- [22] W. C. Zhu, L. L. Niu, S. H. Li, and Z. H. Xu, "Dynamic Brazilian test of rock under intermediate strain rate: pendulum hammer-driven SHPB test and numerical simulation," *Rock Mechanics and Rock Engineering*, vol. 48, no. 5, pp. 1867–1881, 2015.
- [23] J. Zhao, "Modelling of Rock Materials Subjected to Dynamic Loading Using a Particle-Based Numerical Manifold Method (PNMM)," in *International Conference on Analysis of Discontinuous Deformation*, Wuhan, China, October 2015.
- [24] W. C. Zhu and C. A. Tang, "Numerical simulation of Brazilian disk rock failure under static and dynamic loading," *International Journal of Rock Mechanics and Mining Sciences*, vol. 43, no. 2, pp. 236–252, 2006.
- [25] S. Y. Wang, L. Sun, C. Yang, S. Q. Yang, and C. A. Tang, "Numerical study on static and dynamic fracture evolution around rock cavities," *Journal of Rock Mechanics and Geotechnical Engineering*, vol. 5, no. 4, pp. 262–276, 2013.
- [26] Y. F. Yang, C. A. Tang, and K. W. Xia, "Study on crack curving and branching mechanism in quasi-brittle materials under dynamic biaxial loading," *International Journal of Fracture*, vol. 177, no. 1, pp. 53–72, 2012.
- [27] X. Li, M. Tao, F. Gong et al., "Theoretical and experimental study of hard rock spalling fracture under impact dynamic loading," *Chinese Journal of Rock Mechanics & Engineering*, vol. 30, no. 6, pp. 1081–1088, 2011.
- [28] H. Li and L. N. Y. Wong, "Influence of flaw inclination angle and loading condition on crack initiation and propagation," *International Journal of Solids and Structures*, vol. 49, no. 18, pp. 2482–2499, 2012.
- [29] C. Zou and L. N. Y. Wong, "Experimental studies on cracking processes and failure in marble under dynamic loading," *Engineering Geology*, vol. 173, pp. 19–31, 2014.
- [30] C. J. Zou, L. N. Y. Wong, and Y. Cheng, "The Strength and Crack Behavior of the Rock-like gypsum under High Strain Rate," in *ARMA, 46th US Rock Mechanics/Geomechanics Symposium*, pp. 1–15, Chicago, IL, USA, 2012.
- [31] C. Zou, L. N. Y. Wong, J. J. Loo, and B. S. Gan, "Different mechanical and cracking behaviors of single-flawed brittle gypsum specimens under dynamic and quasi-static loadings," *Engineering Geology*, vol. 201, pp. 71–84, 2016.
- [32] X. Li, Z. Tao, and D. Li, "Dynamic strength and fracturing behavior of single-flawed prismatic marble specimens under impact loading with a split-hopkinson pressure bar," *Rock Mechanics & Rock Engineering*, vol. 50, no. 1, pp. 1–16, 2017.
- [33] N. P. Daphalapurkar, K. T. Ramesh, L. Graham-Brady, and J.-F. Molinari, "Predicting variability in the dynamic failure strength of brittle materials considering pre-existing flaws,"

- Journal of the Mechanics and Physics of Solids*, vol. 59, no. 2, pp. 297–319, 2011.
- [34] X.-P. Zhang and L. N. Y. Wong, “Loading rate effects on cracking behavior of flaw-contained specimens under uniaxial compression,” *International Journal of Fracture*, vol. 180, no. 1, pp. 93–110, 2013.
- [35] C. Jiang, G. Zhao, J. Zhu et al., “Investigation of dynamic crack coalescence using a gypsum-like 3D printing material,” *Rock Mechanics and Rock Engineering*, vol. 49, no. 10, pp. 3983–3998, 2016.
- [36] C. Jiang, G. F. Zhao, and N. Khalili, “On crack propagation in brittle material using the Distinct Lattice Spring Model,” *International Journal of Solids and Structures*, vol. 118–119, pp. 41–57, Article ID S0020768317301750, 2017.
- [37] D.-Y. Li, T. Wang, T.-J. Cheng, and X.-L. Sun, “Static and dynamic tensile failure characteristics of rock based on splitting test of circular ring,” *Transactions of Nonferrous Metals Society of China*, vol. 26, no. 7, pp. 1912–1918, 2016.
- [38] Q. B. Zhang and J. Zhao, “Quasi-static and dynamic fracture behaviour of rock materials: phenomena and mechanisms,” *International Journal of Fracture*, vol. 189, no. 1, pp. 1–32, 2014.
- [39] C.-A. Tang and Y.-F. Yang, “Crack branching mechanism of rock-like quasi-brittle materials under dynamic stress,” *Journal of Central South University*, vol. 19, no. 11, pp. 3273–3284, 2012.
- [40] D. J. Frew, M. J. Forrestal, and W. Chen, “A split Hopkinson pressure bar technique to determine compressive stress-strain data for rock materials,” *Experimental Mechanics*, vol. 41, no. 1, pp. 40–46, 2001.
- [41] Z. Y. Liao, J. B. Zhu, K. W. Xia et al., “Determination of dynamic compressive and tensile behavior of rocks from numerical tests of split Hopkinson pressure and tension bars,” *Rock Mechanics & Rock Engineering*, vol. 49, no. 10, pp. 1–18, 2016.
- [42] L. N. Y. Wong and H. H. Einstein, “Crack coalescence in molded gypsum and carrara marble: Part 1. Macroscopic observations and interpretation,” *Rock Mechanics and Rock Engineering*, vol. 42, no. 3, pp. 475–511, 2009.